

OBJECT SHAPE ESTIMATION FROM TOMOGRAPHIC MEASUREMENTS—A PERFORMANCE ANALYSIS*

David J. ROSSI

Schlumberger-Doll Research, Old Quarry Road, Ridgefield, CT 06877-4108, U.S.A.

Alan S. WILLSKY

Department of Electrical Engineering and Computer Science, Massachusetts Institute of Technology, Room 35-233, Cambridge, MA 02139, U.S.A.

Daniel M. SPIELMAN

Information Systems Laboratory, Stanford University, Stanford, CA 94305, U.S.A.

Received 22 August 1988

Revised 18 January 1989

Abstract. The problem considered is that of determining the shape of an object embedded within a medium from noisy tomographic projection measurements. In particular, the issue is addressed of how accurately coarse features of object geometry—size, elongation and orientation—can be characterized from noisy projection data. A maximum likelihood parameter estimation formulation is used and estimation performance is analyzed by evaluation of the Cramer-Rao lower bound on the error variances of the estimates. It is demonstrated that for measurements available at all projection angles and at a given noise level (1) object size and orientation are more accurately determined than is the degree of object elongation, and (2) reliable orientation estimation requires a minimum degree of object elongation, and the required degree of elongation is inversely related to the measurement signal-to-noise ratio (SNR). Based on these observations an iterative algorithm is proposed for estimation of object geometry and results illustrating algorithm performance are presented.

Zusammenfassung. Es wird das Problem betrachtet, die Form eines Objektes zu bestimmen, das von verrauschten tomographischen Daten umgeben wird. Insbesondere wird untersucht, wie genau man die wesentlichen Merkmale der Geometrie der Objekte—Größe, Abstand und Orientierung—aus verrauschten Projektionsdaten bestimmen kann. Die Schätzung der Parameter wird mit der Maximum-Likelihood Methode durchgeführt, die Güte der Schätzung wird mit Hilfe der unteren Cramer-Rao Schranke für die Fehlervarianzen analysiert. Es wird gezeigt, daß für Messungen, die für alle Projektionswinkel verfügbar sind, bei einem festen Rauschpegel (1) Objektgröße und -orientierung genauer bestimmt werden können als ihr Abstand, und daß (2) eine zuverlässige Schätzung der Orientierung einen Mindestabstand der Objekte voraussetzt. Dieser Mindestabstand ist umgekehrt proportional zum Signalrauschverhältnis. Aufgrund dieser Beobachtungen wird ein iterativer Algorithmus zur Schätzung der Objektgeometrie vorgeschlagen, Beispiele zeigen seine Arbeitsweise.

Résumé. On considère le problème de déterminer la forme d'un objet dans une surface. Ceux-ci sont reconstitués à partir de projections tomographiques, en présence de bruit. En particulier, on s'intéresse à savoir avec quelle précision des caractéristiques globales de la géométrie des objets—taille, allongement et orientation—peuvent se tirer de données bruitées. Une formulation de l'estimation de paramètres à vraisemblance maximale (Maximum Likelihood) est utilisée. Les performances de l'estimation sont analysées à l'aide du critère de Cramer-Rao pour l'évaluation de la limite inférieure des variances de l'erreur d'estimation. On démontre deux choses pour des mesures prises à tout angle de projection, en présence d'un niveau de bruit donné. Premièrement, la taille et l'orientation de l'objet se perçoivent de manière plus précise que son degré d'allongement. D'autre part, l'estimation précise de l'orientation nécessite un certain degré d'allongement de l'objet, et le

* This work was supported in part by the National Science Foundation under Grant ECS-8700903 and in part by the Army Research Office under Grant DAAL03-86-K-0171.

degré d'allongement requis est inversement lié au rapport signal sur bruit (SNR) des mesures. Sur la base de ces observations, un algorithme itératif pour l'estimation de la géométrie de l'objet est présenté, ainsi que des résultats illustrant les performances obtenues.

Keywords. Reconstruction, tomography, projection, object, shape, estimation, performance, parametric, maximum likelihood.

1. Introduction

The problem of reconstructing a multi-dimensional function from its projections arises in a diversity of disciplines, typically in imaging applications. In these applications, one is interested in determining a profile characterizing the interior of a medium (e.g., x-ray attenuation coefficient) from integral or projection-type measurements obtained by external probing of the medium.

One popular application is medical x-ray CAT scanning, where x-rays are directed along a collection of straight lines lying in a plane intersecting the patient; the set of projection measurements so obtained are used to reconstruct the x-ray attenuation profile within the cross-section. Recently, a number of novel applications of similar reconstruction techniques have been explored, for example mesoscale oceanographic thermal mapping, quality control nondestructive evaluation, geophysical tomography and “stop action” imaging of very rapidly changing media [3, 4, 6, 7, 9]. In contrast to medical CAT scanning, many of these applications are characterized by measurement limitations due, for example, to limitations in the number of measurement transducers, constraints on measurement time, or operational constraints limiting measurement view angle and/or SNR. These represent severe restrictions when the goal is to produce high resolution, artifact-free cross-sectional imagery, for it is well known that when the projection measurements are limited or noisy, the reconstruction inverse problem is ill-posed, having a numerically sensitive or noisy solution [10].

In a number of applications, particularly with limited measurement data, the *ultimate* goal of the processing is far more modest than obtaining high resolution cross-sectional imagery. More typically the objective involves quantitative and/or qualitative assessment of objects, regions or boundaries within the cross-section, e.g., thermal regions in ocean mapping, cracks and flaws in nondestructive material evaluation and certain anatomical features in medical scanning [6, 15, 17]. The focus of this paper is on the processing of limited or noisy tomographic projection data when the goals involve characterizing *objects* or *regions* in the medium. We model the unknown medium as the superposition of a background medium and one or more local variations in the medium corresponding to objects. Furthermore each object is characterized by a small set of parameters corresponding, for example, to object location, size, and boundary shape. This type of representation has previously been used to analyze the problem of locating an object from tomographic measurements [11, 12], where it was shown that the accuracy of object localization is characterized by a threshold behavior—for a given measurement geometry and measurement noise level, one can identify the smallest size of object that can be reliably located.

In the present paper, that work is extended to the problem of determining, from noisy projection measurements obtained by probing the exterior of a medium, the geometry of an object embedded within the medium. One question to be addressed is how accurately object geometry can be characterized from full-view data (projection measurements acquired from views completely surrounding the object); the limited view angle may be considered in a similar way. To establish insight, attention is focused in this paper on three attributes characterizing coarse object geometry, specifically size, elongation and orientation. These object attributes are considered as unknown quantities which are estimated directly from noisy

tomographic data using maximum likelihood (ML) parameter estimation. The statistical accuracy of these estimates is then characterized by evaluating the Cramer–Rao lower bound (CRLB) on the estimate error variances.

Although the model under consideration is simple, it affords insight into the problem of characterizing object geometry from tomographic data. For example, this analysis may be used to identify, for a given measurement geometry and noise level, the minimum degree of object elongation required to achieve a specified accuracy in object orientation estimation. This analysis also demonstrates that when all three attributes—size, elongation, and orientation—are simultaneously unknown, size and orientation can be estimated substantially more accurately than can the degree of elongation.

The paper is organized as follows. In Section 2, notation is reviewed for both the tomographic reconstruction problem and for the object-based profile model described in [11, 12]. In Section 3 the profile model from [11, 12] is restricted to objects capturing the three features of object geometry already mentioned—size, elongation and orientation. In Section 4 the problem is considered of ML estimation of the object geometry parameters and expressions are obtained for the log likelihood and ambiguity functions which are used to characterize estimation performance. In Section 5 the problem is specialized to the analytically tractable case of Gaussian objects and estimation accuracy is assessed for the individual problems of estimating size, elongation, and orientation. Section 6 illustrates the use of ambiguity functions in the evaluation of the robustness of the estimates of object geometry parameters to modeling errors. The results of these analyses suggest a particular structure for an iterative algorithm for object estimation. In Section 7 we present this algorithm and illustrate its performance characteristics. Conclusions are presented in Section 8.

2. Background

We begin by reviewing the reconstruction of a two-dimensional (2-D) function from its projections. Let $f(x)$ represent the value of the cross-sectional function (for example, x-ray attenuation coefficient) at a point specified by the vector $x = (x_1, x_2)'$. The *projection* of $f(x)$ at angle θ is a 1-D function $g(t, \theta)$ as shown in Fig. 1, which for given values of t and θ is the integral

$$g(t, \theta) = \int_{-\infty}^{\infty} \int_{-\infty}^{\infty} f(x) \delta(t - x' \Theta) dx_1 dx_2 = \int_{x' \Theta = t} f(x) ds \doteq [Rf](t, \theta) \quad (1)$$

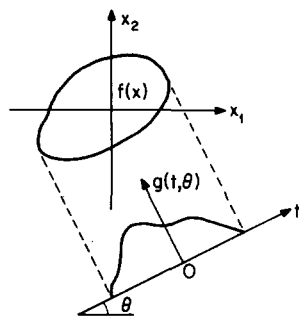


Fig. 1. Projection at angle θ .

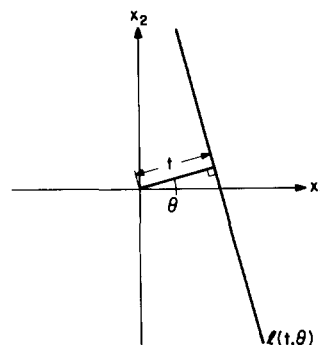


Fig. 2. Measurement ray geometry.

along the line

$$\ell(t, \theta) = \{\mathbf{x}: x_1 \cos \theta + x_2 \sin \theta = t\} = \{\mathbf{x}: \mathbf{x}'\Theta = t\}, \quad (2)$$

$$\Theta \doteq (\cos \theta \quad \sin \theta)', \quad (3)$$

$$(t, \theta) \in S \doteq \{(t, \theta): -\infty < t < \infty, 0 \leq \theta < \pi\}, \quad (4)$$

as shown in Fig. 2. In (1), $\delta(t)$ is the Dirac delta function. The integral equation (1) corresponds to the Radon transformation, which maps the 2-D function $f: \mathbb{R}^2 \rightarrow \mathbb{R}$ into a function on a half-cylinder $g: S \rightarrow \mathbb{R}$; $g(t, \theta)$ is called the Radon transform of $f(\mathbf{x})$, and is also denoted by $[\mathbf{R}f](t, \theta)$.

The convolution backprojection (CBP) inversion formula [13] is one solution to the integral equation in (1); it assumes the availability of noise-free measurements at all (t, θ) values on the half-cylinder S , and is given by

$$\hat{f}(\mathbf{x}) = \int_0^\pi \int_{-\infty}^\infty g(t, \theta) v(t - \mathbf{x}'\Theta, \theta) dt d\theta = \int_0^\pi q(\mathbf{x}'\Theta, \theta) d\theta \doteq [\mathbf{B}q](\mathbf{x}), \quad (5)$$

where the convolving kernel $v(t, \theta)$ is θ -independent with a Fourier transform with respect to t satisfying $V(\omega) = |\omega|$. The so-called *backprojection* operator (the integral with respect to θ) maps the function $q: S \rightarrow \mathbb{R}$ into the 2-D function $\hat{f}: \mathbb{R}^2 \rightarrow \mathbb{R}$; $\hat{f}(\mathbf{x})$ is called the backprojection of q and is also denoted by $[\mathbf{B}q](\mathbf{x})$.

In the object-based model from [11, 12], the 2-D cross-section $f(\mathbf{x})$ is represented as the superposition of a background and N objects,

$$f(\mathbf{x}) = f_b(\mathbf{x}) + \sum_{k=1}^N d_k f(\mathbf{x} - \mathbf{c}_k; \gamma_k). \quad (6)$$

Here, the k th object is located at the point \mathbf{c}_k and has contrast or density d_k (f is normalized so that $f(\mathbf{0}; \gamma_k)$ is unity). The density fluctuations of the k th object are characterized by the finite-dimensional vector of parameters γ_k containing, for example, information about the object boundary shape and interior density fluctuations. The problem of estimating the object location \mathbf{c}_k from noisy projection measurements was considered previously [11, 12].

In this paper, the problem of estimating the object geometry parameters γ_k from noisy projection data is considered. For simplicity, and in order to establish insight, it is assumed that the background $f_b(\mathbf{x})$ is known (and without loss of generality taken to equal zero) and that only a single object ($N = 1$) is present at a known location \mathbf{c}_1 . The single object in the cross-section is considered to have unknown size, shape and orientation (i.e. γ is unknown) and these parameters are estimated directly from noisy tomographic data. In Sections 3–5, the parameterization of object size, shape and orientation is discussed, and the performance of ML estimation of the geometry parameters is evaluated. The effect of errors in various modeling assumptions is a question of robustness, the analysis of which is addressed in detail in [11] and illustrated in Section 6.

3. Representation of object shape

There are various ways to characterize the boundary of an object. For example, if the object is convex, its boundary can be parameterized by the coefficients in a series expansion of its support function [14, 17]; alternatively, an object boundary may be approximately represented by a sequence of horizontally and vertically directed edge elements [2]. In the present analysis, a parameterization is considered that captures

in a simple way three important features of object geometry—size, elongation and orientation. In particular, the object under consideration is approximated as resulting from a simple circularly-symmetric *reference* object by the application of a series of spatial deformations—magnification (size attribute), stretching (elongation attribute) and rotation (orientation attribute).

More specifically, consider a circularly-symmetric *reference* object located at the origin; let it be denoted by $s(x)$, or since it is circular,¹ by $s_p(r)$ in terms of the radial polar coordinate r . The Radon transform of this object is independent of the projection angle θ and is denoted by $g_s(t)$. The energy in the Radon transform is denoted by

$$\xi_s = \int_0^\pi \int_{-\infty}^\infty g_s^2(t, \theta) dt d\theta = \pi \int_{-\infty}^\infty g_s^2(t) dt. \quad (7)$$

The object whose projections are measured is not necessarily circular; it is approximated by the function $d \cdot f(x)$, where $f(x)$ is an elongated object having elliptical contour lines. A circle can be deformed into an ellipse by linear coordinate transformation, and similarly, an appropriately chosen reference function $s(x)$ can be deformed into the approximating object $f(x)$ by linear coordinate transformation, that is, $f(x) = s(Ax)$ where A is a 2×2 matrix. For our purposes, we consider coordinate transformations that can be represented as $A = A_3 A_2 A_1$, i.e. as the composite of up to three successive linear transformations:

- (1) Isotropic scaling of the coordinate system by a *size* factor R ,

$$A_1 = \begin{bmatrix} 1/R & 0 \\ 0 & 1/R \end{bmatrix}, \quad 0 < R < \infty. \quad (8)$$

- (2) Orthogonal stretching and compressing of the coordinate system to transform circular contours into ellipses with *eccentricity* (ratio of major to minor axes lengths) equal to λ ,

$$A_2 = \begin{bmatrix} 1/\sqrt{\lambda} & 0 \\ 0 & \sqrt{\lambda} \end{bmatrix}, \quad 1 < \lambda < \infty. \quad (9)$$

- (3) Rotation of the coordinate system by the *orientation* angle ϕ ,

$$A_3 = \begin{bmatrix} \cos \phi & \sin \phi \\ -\sin \phi & \cos \phi \end{bmatrix}, \quad -\frac{\pi}{2} \leq \phi < \frac{\pi}{2}. \quad (10)$$

As an example of these transformations, consider the reference function $s(x)$ to be an indicator or characteristic function on a unit-radius disk centered on the origin. Then $d \cdot f(x; R, \lambda, \phi)$, the object resulting from the composite of the three coordinate transformations in (8)–(10), is a function that is zero everywhere except on an ellipse centered at the origin, where it takes on the constant value d . Note that the reference function $s(x)$, or $s_p(r)$ in polar coordinates, is not restricted to being constant-valued; it may, for example, be a Gaussian object, $s_p(r) = \exp(-r^2)$.

Summarizing, the cross-section whose tomographic projections are measured is modeled as containing the object $d \cdot f(x; R, \lambda, \phi)$, which is the result of linear coordinate transformation (scaling, stretching, and rotation) of a specified circular object $s(x)$. The focus of this paper is to evaluate how accurately the parameters characterizing size R , eccentricity λ , and orientation ϕ can be estimated from noisy tomographic data. A number of the results obtained in the remainder of this paper are expressed in terms of 2-D Fourier transforms of objects, particularly objects resulting from the scaling, stretching and/or rotation

¹ Because the circularly-symmetric reference object $s(x)$ has circular contours $\{x: s(x) = \text{constant}\}$, it is hereafter referred to as *circular*.

coordinate transformations in (8)–(10). For convenience, the relevant Fourier transform relationships [1] are summarized in Tables 1 and 2.

Table 1

Coordinate transformations in the spatial domain

	Cartesian coordinates	Polar coordinates
Original function	$s(x_1, x_2)$	$s_p(r, \varphi)$
Size transformation A_1 in (8)	$s(x_1/R, x_2/R)$	$s_p(r/R, \varphi)$
Eccentricity transformation ^a A_2 in (9)	$s(x_1/\sqrt{\lambda}, \sqrt{\lambda}x_2)$	$s_p(rh^{-1}(\lambda, \varphi), \tan^{-1}(\lambda \tan \varphi))$
Orientation transformation A_3 in (10)	$s(x_1 \cos \phi + x_2 \sin \phi, -x_1 \sin \phi + x_2 \cos \phi)$	$s_p(r, \varphi - \phi)$

$$^a h(\lambda, \varphi) = (\lambda \cos^2 \varphi + \lambda^{-1} \sin^2 \varphi)^{1/2}.$$

Table 2

Coordinate transformations in the frequency domain

	Cartesian coordinates	Polar coordinates
Original function	$S(\omega_1, \omega_2)$	$S_p(\rho, \psi)$
Size transformation A_1 in (8)	$R^2 S(R\omega_1, R\omega_2)$	$R^2 S_p(R\rho, \psi)$
Eccentricity transformation ^a A_2 in (9)	$S(\sqrt{\lambda}\omega_1, \omega_2/\sqrt{\lambda})$	$S_p(\rho h(\lambda, \psi), \tan^{-1}(\frac{1}{\lambda} \tan \psi))$
Orientation transformation A_3 in (10)	$S(\omega_1 \cos \phi + \omega_2 \sin \phi, -\omega_1 \sin \phi + \omega_2 \cos \phi)$	$S_p(\rho, \psi - \phi)$

$$^a h(\lambda, \varphi) = (\lambda \cos^2 \varphi + \lambda^{-1} \sin^2 \varphi)^{1/2}.$$

The object $d \cdot f(x; R, \lambda, \phi)$ resulting from the coordinate transformations has a Radon transform denoted by $d \cdot g(t, \theta; R, \lambda, \phi)$. As shown in Appendix A, the energy of this Radon transform may be written in terms of ξ_s , the Radon transform energy of the symmetric reference object $s(x)$, as

$$\xi(d, R, \lambda) = d^2 \int_0^\pi \int_{-\infty}^\infty g^2(t, \theta; R, \lambda, \phi) dt d\theta = d^2 R^3 q(\lambda) \xi_s. \quad (11)$$

The Radon transform energy depends on object eccentricity as

$$q(\lambda) = \frac{2}{\pi} \int_0^{\pi/2} \frac{1}{h(\lambda, \phi)} d\phi, \quad (12)$$

where

$$h(\lambda, \phi) = [\lambda \cos^2 \phi + \lambda^{-1} \sin^2 \phi]^{1/2}. \quad (13)$$

Note that $q(\lambda) = q(\lambda^{-1})$ and $q(1) = 1$; the Radon transform energy dependence on eccentricity $q(\lambda)$ is plotted in Fig. 3.

4. Maximum likelihood parameter estimation

Let the noisy projection measurements be given by

$$y(t, \theta) = d \cdot g(t, \theta; R, \lambda, \phi) + w(t, \theta), \quad (14)$$

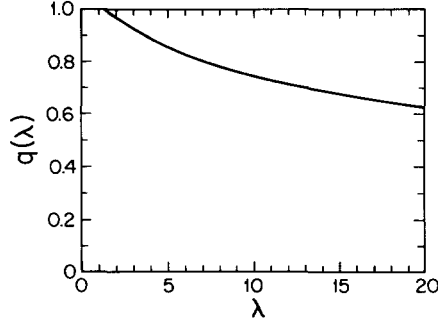


Fig. 3. Radon transform energy dependence on eccentricity λ .

where measurements are taken at all points on the half-cylinder S defined in (4); $w(t, \theta)$ is a zero-mean white Gaussian noise process with spectral level $N_o/2$ [18]. The problem of characterizing the object geometry from noisy tomographic measurements may now be stated as: *given* noisy measurements of the Radon transform as shown in (14), *estimate* the object density d , size R , eccentricity λ , and orientation ϕ . It should be noted that, with the exception of the density factor d , these parameters enter the problem nonlinearly and lead to a nonlinear estimation problem of small dimensionality. This is in contrast to full image reconstruction, in which a linear estimation problem of high dimensionality is solved.

We consider now the problem of ML estimation of the three parameters R , λ , and ϕ that characterize the object's size, elongation and angular orientation. ML estimates of these parameters are the values that maximize the log likelihood function [18]

$$L(R, \lambda, \phi; Y) = \frac{2d}{N_o} \int_0^\pi \int_{-\infty}^{\infty} y(t, \theta) g(t, \theta; R, \lambda, \phi) dt d\theta - \frac{d^2}{N_o} \int_0^\pi \int_{-\infty}^{\infty} g^2(t, \theta; R, \lambda, \phi) dt d\theta. \quad (15)$$

The log likelihood function is the sum of two terms, the first of which is the result of 2-D matched filtering of the measurements $y(t, \theta)$ with the Radon-space (i.e. (t, θ) coordinate system) filtering template $g(t, \theta; R, \lambda, \phi)$ and the second of which compensates for the energy in the Radon-space matched filtering template.

In order to compare the estimated and actual parameter values, let R_a , λ_a , ϕ_a denote the actual object parameters and $g(t, \theta; R_a, \lambda_a, \phi_a)$ the Radon transform of the actual object. The *ambiguity function*, or expected value of the log likelihood function, is given by²

$$a(R, \lambda, \phi; R_a, \lambda_a, \phi_a) = \frac{2d^2}{N_o} \int_0^\pi \int_{-\infty}^{\infty} g(t, \theta; R_a, \lambda_a, \phi_a) g(t, \theta; R, \lambda, \phi) dt d\theta - \frac{d^2}{N_o} \int_0^\pi \int_{-\infty}^{\infty} g^2(t, \theta; R, \lambda, \phi) dt d\theta. \quad (16)$$

As shown in Appendix B, the ambiguity function depends on object size R only through the ratio R/R_a and depends on object orientation ϕ only through the difference $\Delta\phi \doteq \phi - \phi_a$. It may be written as the

² This formulation and the subsequent analysis may be extended to the case of limited view angle (continuous but limited angular coverage in θ) through the introduction of a Radon space window or sampling function such as $\xi_\Delta(t, \theta)$ in Appendix A of [12].

product of an SNR measure and a normalized ambiguity function,

$$a(R, \lambda, \phi; R_a, \lambda_a, \phi_a) = \frac{\xi_a}{N_o} a^*(R/R_a, \lambda, \lambda_a, \Delta\phi). \quad (17)$$

Here ξ_a is the energy in the Radon transform of the actual object. From (11)

$$\xi_a = d^2 R_a^3 q(\lambda_a) \xi_s \quad (18)$$

and the normalized ambiguity function is given by

$$a^*(R/R_a, \lambda, \lambda_a, \Delta\phi) = \frac{2}{q(\lambda_a) \xi_s} \left(\frac{R}{R_a}\right)^2 \int_0^\pi \int_{-\infty}^\infty S_p(\rho h(\lambda_a, \psi)) S_p\left(\frac{\rho R}{R_a} h(\lambda, \psi + \Delta\phi)\right) d\rho d\psi - \frac{q(\lambda)}{q(\lambda_a)} \left(\frac{R}{R_a}\right)^3. \quad (19)$$

In this expression, $q(\cdot)$ is the Radon-space energy dependence on object eccentricity given in (12), and $S_p(r)$ is the Hankel transform of $s_p(r)$, i.e. a central section of the 2-D Fourier transform of $s(\mathbf{x})$.

The ambiguity function plays a key role in performance evaluation for parameter estimation problems. In particular, the CRLB is computationally obtained by evaluating the inverse of the second partial derivative of the ambiguity function at its peak. What this corresponds to is a linearized error analysis assuming that the estimate is not far from the true parameter value. For linear estimation problems the ambiguity function is quadratic and the CRLB in fact yields the exact error variance. For nonlinear problems, such as those considered here, the ambiguity function is not quadratic and indeed does not fall off nearly as quickly away from the peak. Thus typically there is an increased probability that the measurement noise may cause the ML estimates to occur at a likelihood function peak situated far from the true parameter values; in this case, the estimate has large error and is said to be *anomalous*. The probability of obtaining an anomalous estimate may also be characterized from knowledge of the ambiguity function [11, 12, 18]. In what follows we will display the ambiguity functions and will focus our detailed analysis on the CRLB computation which is relevant in the case of moderate to small noise levels.

The expressions developed thus far apply for an arbitrary choice of the circular reference object $s_p(r)$. In the following section, the problem of ML geometry estimation is examined in more detail for the analytically tractable case of Gaussian objects. Furthermore, to simplify the interpretation and develop insight into the problem of estimating object geometry from tomographic data, the three-parameter problem is considered as three separate sub-problems with one parameter unknown at a time. The object size estimation problem is considered first in which the object is taken to be circular ($\lambda = \lambda_a = 1$ and $\Delta\phi = 0$). The eccentricity estimation problem is then considered in which the size and orientation are taken to be known ($R = R_a$ and $\Delta\phi = 0$). Finally, the orientation estimation problem is considered in which object size and eccentricity are assumed to be known ($E = R_a$ and $\lambda = \lambda_a$).

5. Gaussian object

The log likelihood and ambiguity functions presented in the previous section are evaluated in this section for the case of Gaussian objects (see [11] for some extensions to more general objects). Begin with the circular *Gaussian* reference object

$$s_g(r) = \exp(-r^2). \quad (20)$$

The Hankel transform of $s_g(r)$ is

$$S_g(\rho) = \pi \exp(-\pi^2 \rho^2) \quad (21)$$

and the energy in the Radon transform of $s_g(r)$ is

$$\xi_g = \sqrt{\pi/2} \pi^2. \quad (22)$$

By substituting (21) and (22) into (19), and noting that

$$\int_0^\infty e^{-a^2 \rho^2} d\rho = \sqrt{\pi}/2a, \quad (23)$$

an expression is obtained for the Gaussian object normalized ambiguity function

$$a^*(R/R_a, \lambda, \lambda_a, \Delta\phi) = \frac{2\sqrt{2}}{q(\lambda_a)} \left(\frac{R}{R_a}\right)^2 \left[\frac{1}{\pi} \int_0^\pi \{h^2(\lambda_a, \psi) + (R/R_a)^2 h^2(\lambda, \psi + \Delta\phi)\}^{-1/2} d\psi \right] - \frac{q(\lambda)}{q(\lambda_a)} \left(\frac{R}{R_a}\right)^3. \quad (24)$$

5.1. Size estimation

Consider first the problem of using noisy full-view projection measurements to estimate the size of a Gaussian object that results from isotropic coordinate scaling (the coordinate transformation A_1 in (8)) of the circular Gaussian reference object. The size estimation ambiguity function for this case is given by

$$a(R, R_a) = \left(\frac{\xi_a}{N_o}\right) a^*(R/R_a), \quad (25)$$

where ξ_a is the actual object Radon transform energy $d^2 R_a^3 \xi_g$ and $a^*(R/R_a)$ is the special case of the normalized ambiguity function in (24) when $\lambda = \lambda_a = 1$ and $\Delta\phi = 0$. The normalized ambiguity function is plotted in Fig. 4 along with the normalized ambiguity function for the case of a *disk* object (everywhere zero except on a disk of radius R_a , where it takes on a constant value). The close resemblance of these two curves indicates that the ambiguity function for object size estimation is not sensitive to the detailed density variations within the object boundary. Furthermore, these two ambiguity functions attain their maximum value at the true size $R = R_a$ and decrease monotonically and relatively rapidly away from this point. Qualitatively, this suggests good estimation performance, since the peak will not shift significantly with the addition of a small amount of noise.

The CRLB on the size estimate error variance is obtained by evaluating the second partial derivative of the ambiguity function with respect to the parameter R at $R = R_a$. The normalized CRLB on the size estimate error variance is derived in Appendix C and is given by

$$\left(\frac{\sigma_R}{R_a}\right)^2 \geq \frac{2}{11} \frac{N_o}{\xi_a}. \quad (26)$$

This bound on the relative error in the size estimate is simply a constant divided by the SNR. From (18), the Radon space signal energy varies as $d^2 R^3$, so two objects with different sizes but the same value of $d^2 R^3$ are characterized by the same relative error variance of the size estimate. Since signal energy depends on the third power of size R , relative size estimation error variance decreases very rapidly with object size.

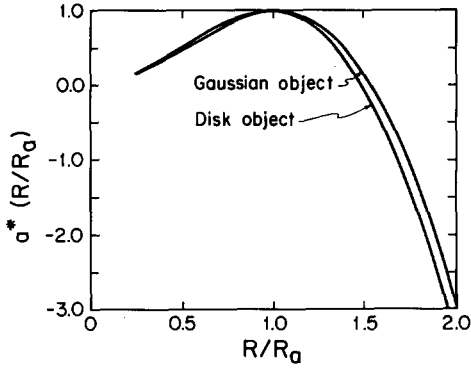


Fig. 4. Normalized size ambiguity functions for Gaussian and disk objects.

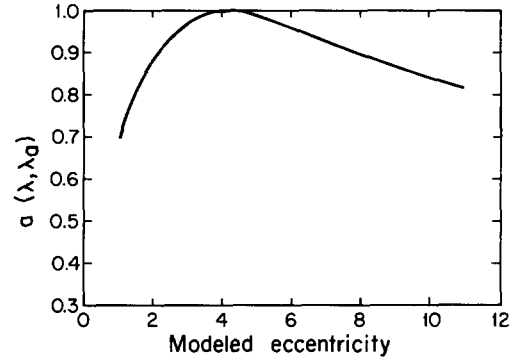


Fig. 5. Normalized eccentricity ambiguity function; $\lambda_a = 4$.

5.2. Eccentricity estimation

Consider now the problem of estimating the eccentricity of a Gaussian object, assuming that all other details such as location, size and orientation are known a priori. For a circular Gaussian object of known size R_a which is elongated by undergoing the coordinate transformation in (9) with an unknown eccentricity factor λ_a , the eccentricity estimation ambiguity function is

$$a(\lambda, \lambda_a) = \frac{\xi_a}{N_o} a^*(\lambda, \lambda_a). \quad (27)$$

Here ξ_a is the actual object Radon transform energy $d^2 R_a^3 q(\lambda_a) \xi_g$ and $a^*(\lambda, \lambda_a)$ is the special case of the normalized ambiguity function in (24) where $R_a = R$ and $\Delta\phi = 0$, which can be reduced to the expression

$$a^*(\lambda, \lambda_a) = \frac{2\sqrt{2}\sqrt{\lambda\lambda_a}q(\sqrt{\lambda\lambda_a})}{\sqrt{\lambda + \lambda_a}q(\lambda_a)} \frac{q(\lambda)}{q(\lambda_a)}. \quad (28)$$

Fig. 5 is a plot of this expression when the actual object eccentricity λ_a is equal to 4. The peak of the ambiguity function occurs at the true parameter value, however, the function does not decrease rapidly away from the true value. Indeed the value of the ambiguity function is within 30% of the peak over a large range of eccentricities. This suggests that accurate estimation of object eccentricity requires a high measurement SNR, even when all other parameters are known perfectly. Also, the slow rate of decrease of the ambiguity function for large eccentricities is indicative of the difficulty in distinguishing the shapes of highly eccentric objects.

The CRLB on the error variance of the eccentricity estimate is obtained by evaluating the second derivative of the ambiguity function with respect to λ at $\lambda = \lambda_a$; the normalized CRLB is given by

$$\begin{aligned} \left(\frac{\sigma_\lambda}{\lambda_a}\right)^2 &\geq \frac{8N_o}{3d^2 R_a^3 \lambda_a^2 \xi_g} \left\{ \frac{2}{\pi} \int_0^{\pi/2} [h(\lambda_a, \psi)]^{-5/2} \left(\cos^2 \psi - \frac{1}{\lambda_a} \sin^2 \psi \right)^2 d\psi \right\}^{-1} \\ &\approx \frac{4}{3} q(\lambda_a) \frac{N_o}{\xi_a} = \frac{4}{3d^2 R_a^3} \frac{N_o}{\xi_g}, \quad \lambda_a \in [1, 20], \end{aligned} \quad (29)$$

where the last line is obtained by numerical evaluation [11]. The lower bound on the relative error variance in the eccentricity estimate is essentially a constant times $q(\lambda_a)$ divided by the SNR. For a fixed noise

level N_o , all objects with the same value of $d^2 R_a^3$ have the same normalized eccentricity estimate error variance, regardless of their eccentricity, i.e. relative eccentricity error variance does *not* decrease as the object becomes more eccentric.

5.3. Orientation estimation

Consider finally the problem of estimating the angular orientation of an elongated Gaussian object from noisy full-view projection measurements. For a circular Gaussian object of known size R_a which undergoes the eccentricity coordinate transformation in (9) with a known eccentricity factor λ_a , and then undergoes the rotation coordinate transformation in (10) with an unknown rotation angle ϕ , the orientation estimation ambiguity function is

$$a(\Delta\phi) = \frac{\xi_a}{N_o} a^*(\Delta\phi). \tag{30}$$

Here ξ_a is the ϕ -independent actual object Radon transform energy $d^2 R_a^3 q(\lambda_a) \xi_g$, and $a^*(\Delta\phi)$ is the special case of the normalized ambiguity function in (24) where $R = R_a$ and $\lambda = \lambda_a$. Note that $a^*(\Delta\phi)$ is symmetric in $\Delta\phi$ (because the eccentric object is centrally-symmetric or balanced) and $a^*(\Delta\phi, \lambda_a) = a^*(\Delta\phi, \lambda_a^{-1})$ since these are ambiguity functions for the same object rotated by 90° . The normalized orientation ambiguity function is plotted in Fig. 6 for several values of actual object eccentricity λ_a . Narrow objects have a more sharply peaked orientation ambiguity function, qualitatively confirming the intuitive notion that the estimation of orientation is more reliable for eccentric as compared to nearly circular objects.

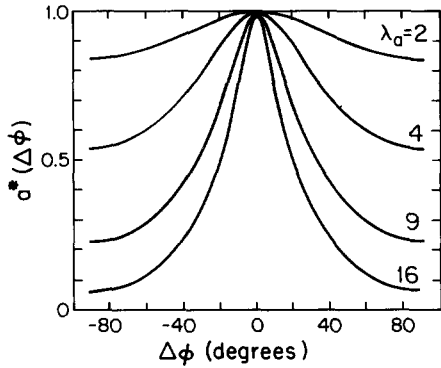


Fig. 6. Normalized orientation ambiguity function for a Gaussian object for several values of eccentricity.

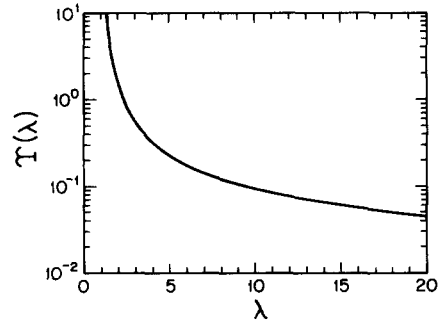


Fig. 7. Normalized orientation Cramer-Rao bound.

This may be expressed more precisely by calculating the CRLB on the orientation estimate error variance, which may be evaluated as the inverse of the second partial derivative of the ambiguity function evaluated at $\phi = \phi_a$,

$$\begin{aligned} \sigma_{\Delta\phi}^2 &\geq \frac{N_o}{\xi_a} q(\lambda_a) \left\{ \frac{3}{8} (\lambda_a^{-1} - \lambda_a)^2 \left[\frac{2}{\pi} \int_0^{\pi/2} h(\lambda_a, \psi)^{-5/2} \sin^2(2\psi) d\psi \right] \right. \\ &\quad \left. + (\lambda_a^{-1} - \lambda_a) \left[\frac{2}{\pi} \int_0^{\pi/2} h(\lambda_a, \psi)^{-3/2} \cos(2\psi) d\psi \right] \right\}^{-1} \\ &\doteq \frac{N_o}{d^2 R^3 \xi_g} Y(\lambda_a). \end{aligned} \tag{31}$$

$Y(\lambda_a)$, the dependence of the error variance bound on object eccentricity, is plotted in Fig. 7. The bound is seen to be a rapidly decreasing function of eccentricity, which is expected since it is easier to estimate the orientation of more eccentric objects. Thus, the CRLB is a decreasing function of both SNR and object eccentricity; this suggests the possibility of adapting the model complexity (number parameters or degrees of freedom) to the measurement quality, which is explored in the following section.

5.4. Selecting the modeled object complexity

Fig. 7 confirms the intuitive notion that the estimate of the angular orientation of the object improves as the object becomes increasingly elongated and with increasing SNR. Conversely, for values of λ_a approaching unity (object contours nearly circular) the bound approaches infinity, that is, a very high SNR is required to estimate the orientation. However, in the case of a nearly circular object, orientation is a far less important parameter than say object size, which could in this case be determined by using a simpler circular object model. Here, we turn this intuitive notion into a precise decision rule for selecting, based on knowledge of the SNR $d^2 R^3 \xi_g / N_o$ and an estimate of object eccentricity $\hat{\lambda}$, between the following two hypotheses:

- H_0 : the object is nearly circular ($\lambda \approx 1$),
 H_1 : the object has an elongated geometry ($\lambda > 1$).

Various criteria may be used to develop a decision rule for these hypotheses, and our criterion is based on the observation that if the available measurements do not provide a high quality orientation estimate (i.e. the error variance is too large), it is more appropriate to assume that the object is circular. In particular, suppose that an a priori limit κ exists on the maximum acceptable value of orientation estimate error variance $\sigma_{\Delta\phi}^2$. The decision rule we propose is to decide H_1 if and only if the bound on the error variance of the orientation estimate does not exceed κ , that is, decide H_1 if and only if:

$$\frac{N_o}{d^2 R^3 \xi_g} Y(\hat{\lambda}) < \kappa \quad (32)$$

or

$$Y(\hat{\lambda}) < \frac{d^2 R^3 \xi_g}{N_o} \kappa \quad (33)$$

or, since $Y(\lambda)$ is a monotonically decreasing function,

$$\hat{\lambda} > Y^{-1} \left\{ \frac{d^2 R^3 \xi_g}{N_o} \kappa \right\} \doteq \lambda_{\min}(\text{SNR}, \kappa). \quad (34)$$

Thus, given a minimum acceptable orientation error variance κ and knowing the measurement SNR, the rule in (34) may be employed to decide, based on the estimated eccentricity $\hat{\lambda}$, whether to use an elliptical model (with a corresponding orientation estimate meeting the accuracy specification κ) or, because sufficient orientation accuracy cannot be insured, to use a simpler circularly symmetric model. An example of this decision rule will be presented in Section 7.

6. Robustness analysis

The ambiguity function analysis we have described can also be used to study robustness of the parameter estimates to various modeling errors. A complete treatment of this topic is given in [11]. We limit ourselves here to a brief illustration which also allows us to draw several important conclusions that lead directly to the algorithm described in the next section. Specifically, we examine here the robustness of both size and orientation estimates to errors in knowledge of object eccentricity.

6.1. Size estimation in the presence of eccentricity errors

In this subsection we examine the robustness of the estimate of object size to errors in knowledge of object eccentricity. The size ambiguity function evaluated in the presence of eccentricity mismatch (i.e. when the modeled and actual eccentricities differ) is a special case of the three parameter ambiguity function in (17) when $\theta = \theta_a = 0$ (the rotation transformation is not applied) and is given by

$$a(R, \lambda, 0, R_a, \lambda_a, 0) = \frac{\xi_a}{N_o} a^*(R/R_a, \lambda, \lambda_a, 0), \tag{35}$$

where a^* is given in (19). Specializing to the case of a Gaussian object yields

$$a^*(R/R_a, \lambda, \lambda_a, 0) = \frac{2\sqrt{2}}{q(\lambda_a)} \left(\frac{R}{R_a}\right)^2 \left[\frac{1}{\pi} \int_0^\pi \left\{ \left(\lambda_a + \left(\frac{R}{R_a}\right)^2 \lambda \right) \cos^2 \psi + \left(\frac{1}{\lambda_a} + \left(\frac{R}{R_a}\right)^2 \frac{1}{\lambda} \right) \sin^2 \psi \right\}^{-1/2} d\psi \right] - \frac{q(\lambda)}{q(\lambda_a)} \left(\frac{R}{R_a}\right)^3 \tag{36}$$

Notice that when $\lambda = \lambda_a = 1$ (circular object), (36) reduces to the size ambiguity function plotted in Fig. 4 and the peak occurs at $R/R_a = 1$.

Fig. 8 displays a^* as a function of object size for five values of λ when the actual object has eccentricity $\lambda_a = 4$. This figure indicates that when the eccentricity is not accurately known a priori, the peak of the size ambiguity function does not occur at $R/R_a = 1$, i.e. the estimate is *biased*. While this shift in the peak

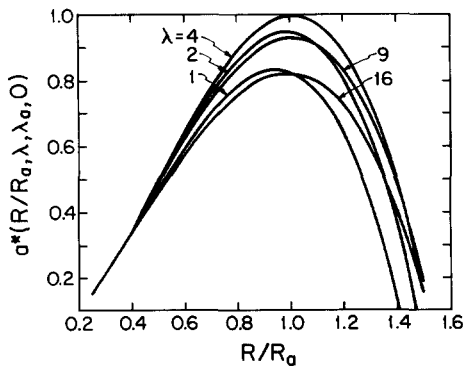


Fig. 8. Normalized size ambiguity function in the presence of eccentricity modeling errors; $\lambda_a = 4$.

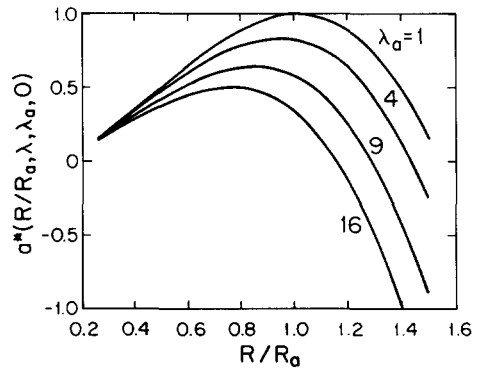


Fig. 9. Normalized size ambiguity function when the modeled object is circular ($\lambda = 1$) but the actual object has eccentricity $\lambda_a = 1, 4, 9$ and 16 .

location with eccentricity modeling error is not negligible, it should be noted that the extent of peak shift is relatively mild—the peak shifts upward by less than 3% when the eccentricity is overmodeled by a factor of 4 and shifts downward by about 7% when eccentricity is undermodeled by a factor of 4 (i.e. when an object with eccentricity 4 is modeled as being circular).

This last case of a circular modeled object is interesting in its own right, since in practice one may have no reason to believe a priori that the object is eccentric. Consequently, it would be reasonable in such a situation to use a circular object model to determine object size. Fig. 9 is a plot of the normalized size ambiguity function in (36) for the case where a circular ($\lambda = 1$) modeled object is used to estimate the size of an actual object that is either circular ($\lambda_a = 1$) or eccentric with $\lambda_a = 4, 9$ or 16. Here, the ambiguity function peak occurs at the true parameter value only when the eccentricity is correctly modeled ($\lambda_a = 1$); when the eccentricity is undermodeled (using a circular model when $\lambda_a = 4, 9$ and 16) the peak location is shifted downward to R/R_a values of 0.94, 0.84 and 0.75 respectively.

Consequently, estimating the size of an eccentric object by using a circular model results in a biased estimate. It should be noted, however, that the amount of bias is relatively modest—modeling an object with eccentricity $\lambda_a = 16$ as being circular represents a very significant modeling error, yet it results in a shift of only 25% in the position of the size ambiguity function peak.

In summary, the ambiguity function in (36), along with Figs. 8 and 9 indicate that an unbiased size estimate is not obtained when the actual object's eccentricity is unknown and is modeled incorrectly. However, the magnitude of the bias in the size estimate is a slowly increasing function of eccentricity, both indicating that useful initial estimates can be obtained using a circular model and suggesting an iterative approach developed in the next section in which a refinement in size estimate can be made after eccentricity is estimated.

6.2. Orientation estimation in the presence of eccentricity errors

In order to obtain a meaningful estimate of eccentricity it is necessary to have a good estimate of orientation. Consequently, an important question concerns our ability to estimate orientation when accurate knowledge of eccentricity is not yet available. In this subsection, we consider the robustness of the orientation estimation problem to errors in the a priori value of object eccentricity. In particular, we evaluate the orientation ambiguity function when the actual and modeled eccentricities differ.

In the presence of eccentricity modeling errors, the orientation ambiguity function is a special case of the three-parameter ambiguity function in (17) when $R = R_a$ and is given by

$$a(R_a, \lambda, \phi; R_a, \lambda_a, \phi_a) = \frac{\xi_a}{N_o} a^*(1, \lambda, \lambda_a, \Delta\phi), \quad (37)$$

where a^* is given in (19). Specializing to the case of a Gaussian object yields

$$a^*(1, \lambda, \lambda_a, \Delta\phi) = \frac{2\sqrt{2}}{q(\lambda_a)} \left[\frac{1}{\pi} \int_0^\pi \left\{ \lambda_a \cos^2 \psi + \lambda \cos^2(\psi + \Delta\phi) + \frac{1}{\lambda_a} \sin^2 \psi + \frac{1}{\lambda} \sin^2(\psi + \Delta\phi) \right\}^{-1/2} d\psi \right] - \frac{q(\lambda)}{q(\lambda_a)}. \quad (38)$$

Fig. 10 displays a^* as a function of $\Delta\phi$ for several values of modeled object eccentricity when the true object satisfies $\lambda_a=4$. Even with eccentricity modeling errors the orientation ambiguity function is symmetric with its peak situated at the true orientation value. Consequently, if one were to hypothesize a value of λ and estimate only the orientation ϕ , the resulting estimate would be unbiased. When a value of eccentricity is selected that is smaller than the true value, the ambiguity function has a broader peak than it does when the true value is used, indicating that the orientation can not be estimated as accurately as it can when the true eccentricity is known. When a value of eccentricity is used that is larger than the true value, the ambiguity function has approximately the same degree of sharpness but the peak value is smaller than it is when the true value is known.

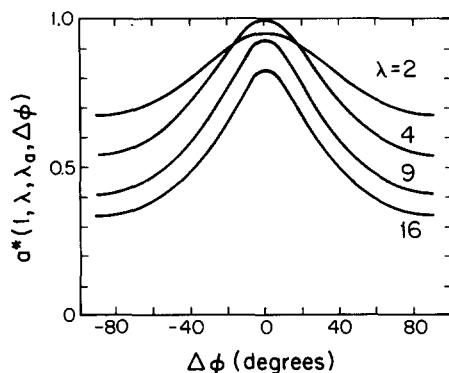


Fig. 10. Normalized orientation ambiguity function in the presence of eccentricity modeling errors; $\lambda_a = 4$.

This suggests that while the best estimation performance is obtained in the matched (eccentricity known) case, orientation estimation performance is relatively insensitive to errors in the a priori eccentricity value. The orientation estimation problem, then, may be approached by using some nominal (but possibly incorrect) value of eccentricity, where, as indicated by Fig. 10, it is preferable to overestimate rather than underestimate the eccentricity.

In this section we have illustrated methods for analyzing the robustness of geometric parameter estimation to modeling errors. A more complete investigation of robustness is presented in [11] corroborating what we have illustrated here, namely that geometric parameter estimation is quite robust to modeling errors. Moreover, the conclusions that can be drawn from the results presented in this section and in [11] suggest a particular iterative algorithm for the simultaneous estimation of several geometric parameters. This is the subject of the following section.

7. Iterative algorithm and experimental results

The analysis presented in the preceding sections and in [11, 12] yields, among others, the following conclusions:

- Object location estimation is extremely robust to errors in modeled object shape, e.g., to errors in assumed object eccentricity and size. In general, less degradation is obtained if object size is overestimated rather than underestimated³ (see [11, 12]).

³ This is intuitively clear since a small object can be centered at many locations and still be completely contained within a larger version of the object.

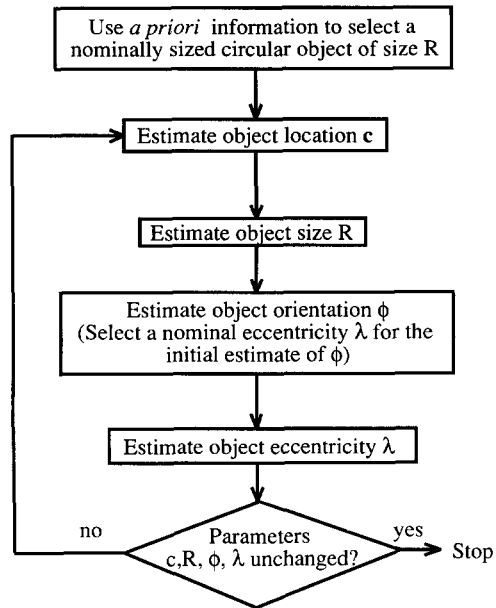
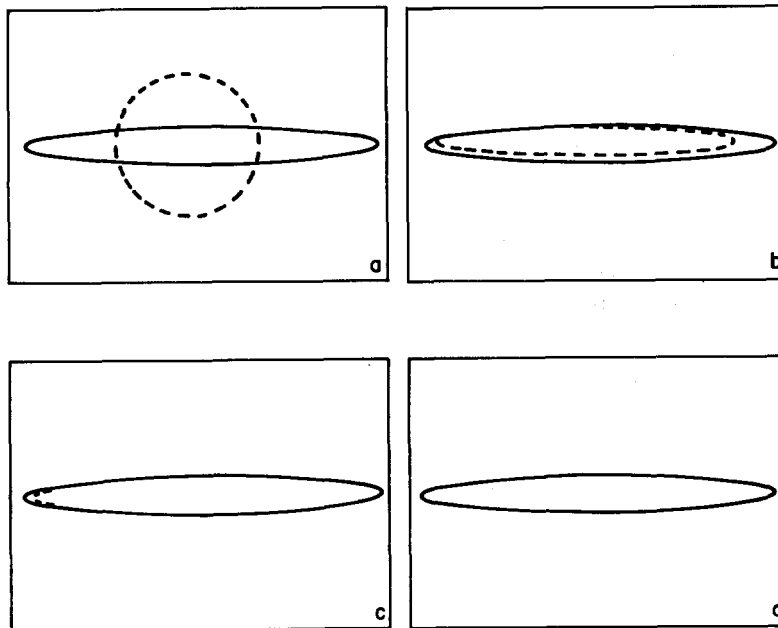


Fig. 11. Flow graph for the iterative single object estimation algorithm.

Fig. 12. Results from intermediate steps of the estimation of an elliptical object with SNR=0 dB. The solid lines represent the actual object ($c = (0, 0)$, $R = 10$, $\lambda = 9$, $\phi = 0^\circ$), and dashed lines correspond to the iterative estimates of the object geometry:

- (a) estimate after localization step: $\hat{c} = (-2.52, 0.42)$, $\hat{R} = 12$, $\hat{\lambda} = 1$, $\hat{\phi} = 0.0^\circ$;
 (b) after one complete iteration: $\hat{c} = (-2.52, 0.42)$, $\hat{R} = 7.8$, $\hat{\lambda} = 10.7$, $\hat{\phi} = 0.0^\circ$;
 (c) after two iterations: $\hat{c} = (1.26, 0.0)$, $\hat{R} = 10.0$, $\hat{\lambda} = 8.6$, $\hat{\phi} = 0.0^\circ$;
 (d) third and final estimate: $\hat{c} = (0.0, 0.0)$, $\hat{R} = 10.0$, $\hat{\lambda} = 9.3$, $\hat{\phi} = 0.0^\circ$.

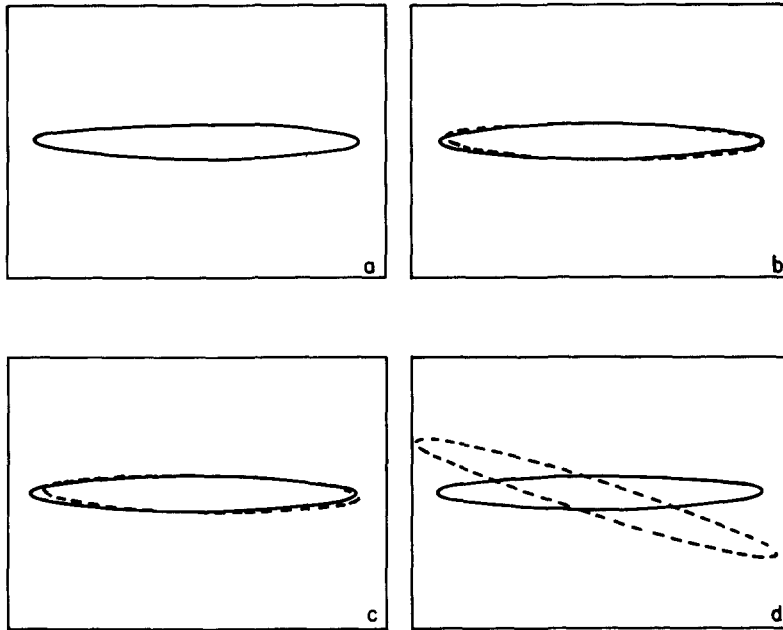


Fig. 13. Estimation of an elliptical object at four SNRs. The solid lines represent the actual object ($c = (0, 0)$, $R = 10$, $\lambda = 9$, $\phi = 0^\circ$), the dashed lines correspond to the final estimated object geometry at four SNRs.:

- (a) SNR = 0 dB, $\hat{c} = (0.0, 0.0)$, $\hat{R} = 10.0$, $\hat{\lambda} = 9.3$, $\hat{\phi} = 0.0^\circ$;
 (b) SNR = -8.7 dB, $\hat{c} = (0.84, 0.0)$, $\hat{R} = 10.0$, $\hat{\lambda} = 9.3$, $\hat{\phi} = 0.0^\circ$;
 (c) SNR = -17.4 dB, $\hat{c} = (1.26, 0.0)$, $\hat{R} = 10.2$, $\hat{\lambda} = 8.2$, $\hat{\phi} = -1.8^\circ$;
 (d) SNR = -26.1 dB, $\hat{c} = (-0.84, -0.84)$, $\hat{R} = 10.4$, $\hat{\lambda} = 11.4$, $\hat{\phi} = -18.0^\circ$.

- Object size estimation has a mild bias in the presence of eccentricity errors which increases very slowly as the extent of this error increases.
- Orientation estimation remains unbiased in the presence of eccentricity errors, and performance improves as eccentricity increases.
- Of the three geometry attributes studied, eccentricity estimation is the most sensitive to noise, orientation errors, etc.
- Estimation of all parameters are robust to errors in the choice of the circular profile.

These observations suggest the following iterative algorithm for the simultaneous estimation of object location, size, orientation and eccentricity.

- Initially assume that the object is a large circular object, and estimate its location⁴. This estimate will be unbiased.
- Given the estimated location, estimate object size still assuming that the object is circular. This estimate may be mildly biased if the object is not circular.
- Given estimates of the object location and size, estimate object orientation assuming a nominal value of eccentricity. This estimate will be unbiased.
- Given estimates of object location, size and orientation, estimate eccentricity.
- Update iteratively the estimates of location, size, orientation and eccentricity (in this order) using the latest estimates of the remaining parameters.

⁴ See [11, 12] for a detailed discussion of ML estimation of object location.

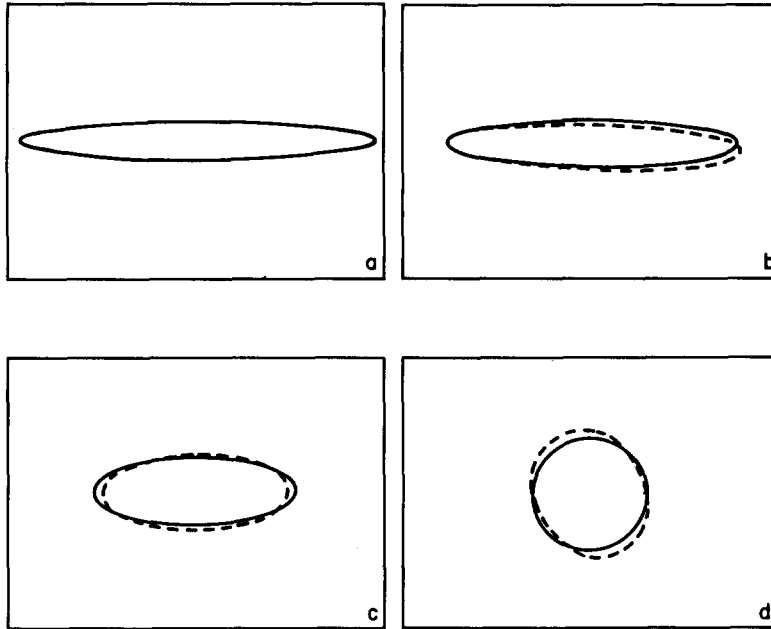


Fig. 14. Final estimation results at 0 dB for elliptical objects having eccentricities $\lambda_a = 9, 6, 3$ and 1. The dashed lines correspond to the final estimated object geometry:

- (a) $\lambda_a = 9$: $\hat{\mathbf{c}} = (0.0, 0.0)$, $\hat{R} = 10.0$, $\hat{\lambda} = 9.3$, $\hat{\phi} = 0.0^\circ$;
 (b) $\lambda_a = 6$: $\hat{\mathbf{c}} = (0.42, -0.84)$, $\hat{R} = 9.8$, $\hat{\lambda} = 6.5$, $\hat{\phi} = -1.8^\circ$;
 (c) $\lambda_a = 3$: $\hat{\mathbf{c}} = (0.0, 0.0)$, $\hat{R} = 10.0$, $\hat{\lambda} = 2.4$, $\hat{\phi} = 1.8^\circ$;
 (d) $\lambda_a = 1$: $\hat{\mathbf{c}} = (0.0, 0.0)$, $\hat{R} = 10.4$, $\hat{\lambda} = 1.2$, $\hat{\phi} = -57.6^\circ$.

A flow graph of this algorithm is given in Fig. 11. Note that this algorithm belongs to a class of optimization algorithms known as *cyclic coordinate descent algorithms* [8], in which each iteration consists of four 1-parameter optimization steps, and each 1-parameter optimization is carried out by line search. In all of the experiments reported here, the initial circular object size R in the first step of the algorithm was taken to be 12 and the initial eccentricity λ in the fourth step was set to 5.

Experimentation with this algorithm has demonstrated that it has excellent convergence properties. Typically, estimates are obtained in a single iteration, and one or two further iterations provide the small amount of fine tuning needed for final conversion. Fig. 12 is representative of the algorithm performance. In this example, the true object is the ellipse shown with the solid line⁵. Measurements at a SNR⁶ of 0 dB are used to produce the estimates shown with dashed lines. Fig. 12(a) shows the result after the very first step of the iteration, i.e. object location estimation assuming that the object is a large circle. While the location estimate is slightly in error, it is quite good. Note that the error is primarily in the horizontal direction which is to be expected since the error in fitting a circle to the data has very little sensitivity to horizontal translations about the true object center. Fig. 12(b) shows the estimate after one full pass through the iteration, i.e. after R , ϕ and λ have been estimated in succession but no re-estimation has been done. Despite the initial location error, the fit is relatively good, with good estimates of ϕ and λ .

⁵ In all of the results described in this section, the circular reference function is an indicator function on a unit-radius disk.

⁶ All experimental results in the section involve a discrete rather than continuous set of measurements. Consequently a discrete definition of SNR is used, namely $\text{SNR} = 20 \log(\epsilon_D/\sigma^2)$, where σ^2 is the variance of each measurement and the signal energy is $\epsilon_D = \sum g^2(t_m, \theta_j)$ where the sum is over all measurements (t_m, θ_j) .

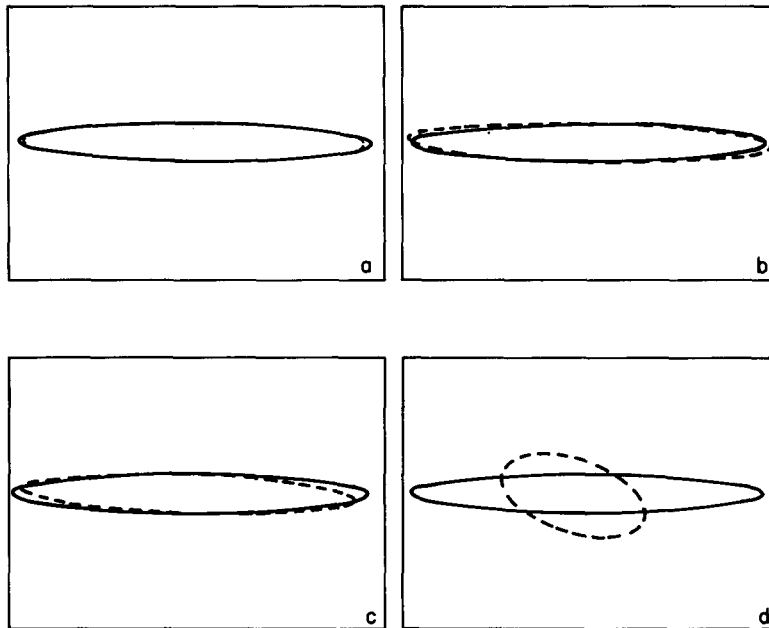


Fig. 15. Estimation results for an elliptical object with a limited amount of 0 dB measurement data. The dashed lines correspond to the final estimated object geometry:

- (a) 45 views, 11 rays/view, $\hat{c} = (0.0, 0.0)$, $\hat{R} = 9.8$, $\hat{\lambda} = 8.8$, $\hat{\phi} = 0.0^\circ$;
 (b) 20 views, 25 rays/view, $\hat{c} = (0.0, 0.0)$, $\hat{R} = 10.2$, $\hat{\lambda} = 9.2$, $\hat{\phi} = -1.8^\circ$;
 (c) 20 views, 11 rays/view, $\hat{c} = (0.0, 0.0)$, $\hat{R} = 9.6$, $\hat{\lambda} = 8.4$, $\hat{\phi} = 1.8^\circ$;
 (d) 5 views, 11 rays/view, $\hat{c} = (-2.10, -0.42)$, $\hat{R} = 8.6$, $\hat{\lambda} = 2.2$, $\hat{\phi} = -18.0^\circ$.

These improved estimates then allow extremely rapid fine tuning of the estimate during the second (Fig. 12(c)) and third (Fig. 12(d)) iterations.

The remaining results described in this section provide a picture of the performance characteristics for this problem. In Fig. 13 we show the effect on the final estimation accuracy of decreasing the SNR—from 0 dB in Fig. 13(a) to -26.1 dB in Fig. 13(d). The behavior seen here is typical of nonlinear estimation problems: as one decreases SNR, one sees a gradual deterioration in performance (Figs. 13(a)—(c)) until a threshold level is reached. For SNRs below this level, there is a significant probability that highly anomalous estimates will be made, as in Fig. 13(d). This provides us with a clear limit over which it makes sense to estimate object shape parameters. Note that because we are only seeking a very small number of degrees of freedom, we can achieve good performance at quite low SNRs.

Fig. 14 illustrates performance as a function of true object eccentricity ($\lambda = 9, 6, 3$ and 1) at a fixed SNR of 0 dB. As predicted by our analysis, the best performance is obtained for highly eccentric objects. As eccentricity decreases toward unity, orientation and eccentricity estimates degrade. Note, however, that the fit error, i.e. the difference between dashed and solid objects, degrades only mildly. This is not surprising, as the sensitivity of the estimated object boundary to orientation errors decreases as eccentricity approaches unity. Indeed in Fig. 14(d), the orientation estimate is essentially irrelevant as the true object is a circle. If we had used the decision rule (34) in this case, we would have decided that the estimated eccentricity of 1.2 was negligibly close to unity and would have rejected the more complex model in favor of fitting a circle. The result in this case is an estimate of object location and size almost identical to the true values, removing essentially all of the remaining fit error present in Fig. 14(d).

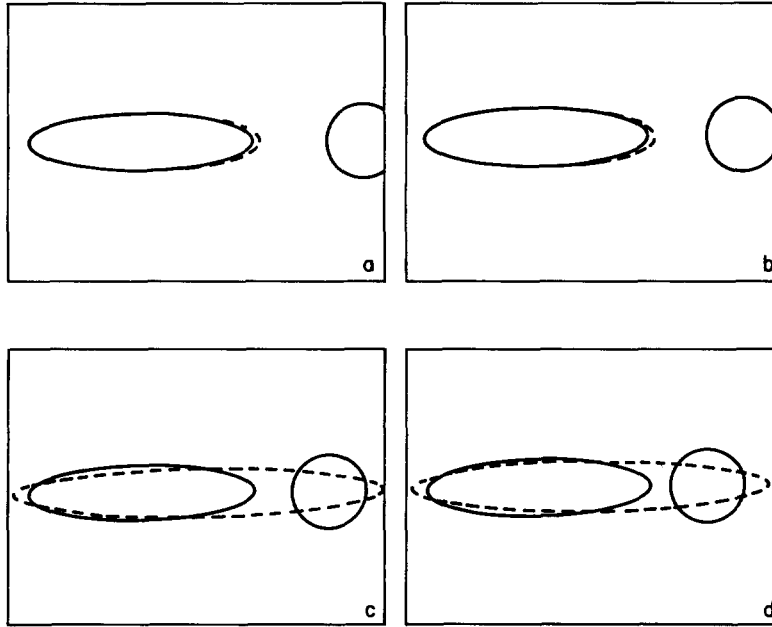


Fig. 16. Estimation of an elliptical object in the presence of an unmodeled circular object, no noise. The solid lines represent the actual elliptical object ($c = (-20, 0)$, $R = 15$, $\lambda = 4$, $\phi = 0^\circ$) and the actual circular object of size $R = 10$, the dashed lines correspond to the final estimates of the object geometry:

- (a) circular object at $c = (40, 0)$: $\hat{c} = (-19.3, 0.0)$, $\hat{R} = 15.4$, $\hat{\lambda} = 4.0$, $\hat{\phi} = 0.0^\circ$;
- (b) circular object at $c = (35, 0)$: $\hat{c} = (-19.3, 0.0)$, $\hat{R} = 15.6$, $\hat{\lambda} = 4.0$, $\hat{\phi} = 0.0^\circ$;
- (c) circular object at $c = (30, 0)$: $\hat{c} = (-4.2, 0.0)$, $\hat{R} = 17.8$, $\hat{\lambda} = 7.8$, $\hat{\phi} = 0.0^\circ$;
- (d) circular object at $c = (25, 0)$: $\hat{c} = (-6.3, 0.0)$, $\hat{R} = 17.8$, $\hat{\lambda} = 7.0$, $\hat{\phi} = 0.0^\circ$.

Although we have not discussed the analysis of this problem, it is possible to use this same algorithm when one has available only limited amounts of data [11, 16]. Fig. 15 illustrates the effect of limited data on estimation accuracy. Figs. 15(a) and 15(b) show estimation performance for two cases in which the total number of line integral measurements are roughly the same (495 in (a), 500 in (b)), but they are distributed differently in t and θ . Specifically in Fig. 15(a) we use a greater number of viewing angles (45 vs. 20) and fewer line integrals per view (11 vs. 25). Comparing these two figures we see that better performance is achieved if greater angular diversity is used. This is further emphasized in the remaining figures. In particular, Fig. 15(c) uses the same number of viewing angles as in Fig. 15(b), but less than half the measurements per view. There is only very slight performance loss, indicating the low sensitivity to the number of measurements per view. In Fig. 15(d), the angular diversity has been drastically reduced—only 5 views—and as can be seen, at this point there is not enough angular information to obtain a reasonable fit.

Finally, in Figs. 16 and 17 we present some results indicating the level of robustness to the presence of additional objects in the field of view when the parameters for only one object are being estimated⁷.

⁷ In the presence of multiple objects, one could proceed with an N -object formulation as shown in (6), in which case the Radon transform in (1) would be a sum over N objects and the log likelihood function in (15) would contain sums over N objects, where R , λ and ϕ would be N -vectors. A simultaneous fit to all N objects could then be carried out as a direct maximization of the corresponding log likelihood function. In a case where two or more objects of similar energy are situated in close proximity, a multiple object formulation is preferred.

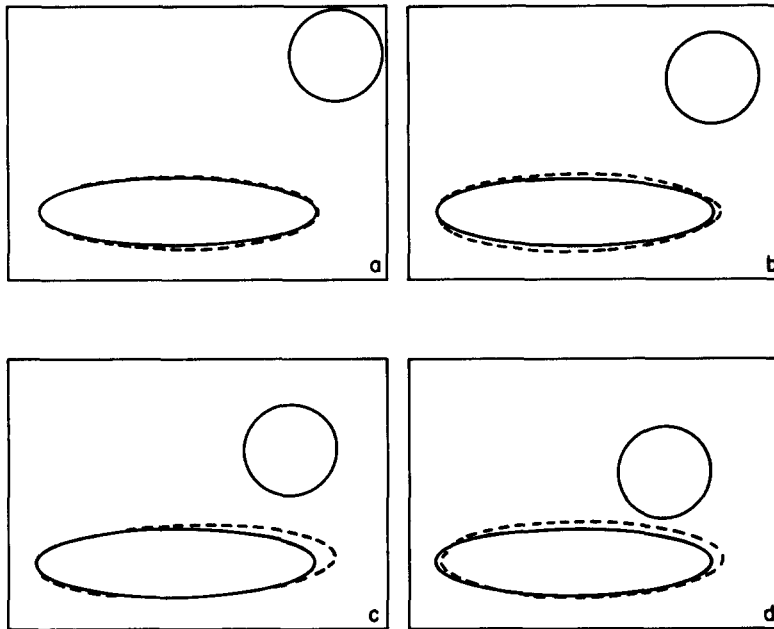


Fig. 17. Estimation of an elliptical object in the presence of an unmodeled circular object centered along a ray $\phi = \pi/4$, no noise. The solid lines represent the actual elliptical object ($c = (-20, 0)$, $R = 15$, $\lambda = 4$, $\phi = 0^\circ$) and the actual circular object of size $R = 10$, the dashed lines correspond to the final estimates of the object geometry:

- (a) circular object at $c = (15, 35)$: $\hat{c} = (-19.7, 0.0)$, $\hat{R} = 15.6$, $\hat{\lambda} = 3.8$, $\hat{\phi} = 0.0^\circ$;
- (b) circular object at $c = (10, 30)$: $\hat{c} = (-19.7, 0.0)$, $\hat{R} = 16.0$, $\hat{\lambda} = 3.6$, $\hat{\phi} = 0.0^\circ$;
- (c) circular object at $c = (5, 25)$: $\hat{c} = (-18.1, 0.42)$, $\hat{R} = 16.4$, $\hat{\lambda} = 4.0$, $\hat{\phi} = 1.8^\circ$;
- (d) circular object at $c = (0, 20)$: $\hat{c} = (-18.5, 0.8)$, $\hat{R} = 16.4$, $\hat{\lambda} = 3.6$, $\hat{\phi} = 0.0^\circ$.

In each figure the larger object is an ellipse of size $R = 15$ and the smaller object is a circle of size $R = 10$. Note that the circle is not particularly small compared to the ellipse, although its Radon space energy is one third that of the ellipse. In each figure we show results of noise-free estimation of a single elliptical object when the true density field consists of the two objects, with varying center-to-center separations. In Fig. 16 the circular object is aligned with the major ellipse axis at a distance that decreases from Figs. 16(a)–(d). For moderate distances, estimation performance is affected in only a minor way. As the circle is moved closer, however, the significant amount of circle Radon space energy, especially in the vertical and near-vertical projections, causes the estimate to attempt to fit both objects at once. This provides us with an indication of inter-object spacings that can be tolerated without resorting to additional procedures (such as detecting the gap in the vertical projections corresponding to line integrals between objects). Note that Fig. 16 is in fact a worst-case situation, as the circle is aligned with the ellipse's major axis. In Fig. 17, the circle is centered along a line that is at 45° to horizontal. In this case the fit to the ellipse is only mildly affected even for very close spacings between the objects.

8. Conclusions

The problem has been considered of estimating the size, eccentricity and orientation of an object within a cross-section of a 2-D medium from noisy tomographic data, i.e. noisy observations of the Radon

transform. The object in the cross-section has been modeled as the result of applying one or more of the linear coordinate transformations in (8)–(10) to a circular reference object, with the coordinate transformations parameterized by three variables corresponding to object size, eccentricity and orientation. ML estimation of these parameters was investigated via evaluation of the ambiguity function and the CRLB on the estimate error variance, and results were illustrated for the class of Gaussian objects. It was demonstrated that for measurements available at all projection angles and at a given noise level, (1) object size and orientation can be estimated more accurately than the degree of object elongation and (2) reliable orientation estimation requires a minimum degree of object elongation, and the required degree of elongation is inversely related to the measurement SNR. This result was used to derive a simple decision rule for selecting the appropriate complexity of the modeled object (circular versus elongated).

We have also presented some analysis of the robustness of the ML geometry estimation procedure to modeling errors such as incorrect knowledge of object location and eccentricity. Further results along these lines may be found in [11]. Generally, geometry parameter estimation has been found to be quite robust to a variety of modeling errors. Based on this analysis, we have developed an iterative algorithm for geometry estimation and have demonstrated its efficiency. We have also presented results illustrating the performance characteristics for this problem. These results both indicate the inherent robustness of this problem and also provide clear indications of the range of situations in which such a procedure is effective.

Acknowledgments

The authors would like to thank the reviewers for their helpful comments and suggestions.

Appendix A. Radon-space energy of an eccentric object

The Radon-space energy $\xi(d, R, \lambda)$ in (11), which is independent of the object orientation parameter ϕ , is given by

$$\xi(d, R, \lambda) = d^2 \int_0^\pi \int_{-\infty}^{\infty} g^2(t, \theta; R, \lambda, \phi) dt d\theta. \quad (\text{A.1})$$

By the definition of the back-projection operator defined in (5), this may be written as

$$\xi(d, R, \lambda) = d^2 [\mathbf{B}(g * g)](x)|_{x=0}, \quad (\text{A.2})$$

where $*$ denotes 1-D convolution in the t variable. Noting that g is the Radon transform of f as defined in (1),

$$\xi(d, R, \lambda) = d^2 [\mathbf{B}(\mathbf{R}f * \mathbf{R}f)](x)|_{x=0} = d^2 \left[f ** f ** \frac{1}{|r|} \right](x)|_{x=0}, \quad (\text{A.3})$$

where $**$ denotes 2-D convolution, and the last line follows from repeated application of the equality [5, 12]

$$[\mathbf{B}(\mathbf{R}f * \nu)](x) = [f ** \mathbf{B}\nu](x). \quad (\text{A.4})$$

That is, the CBP of $[\mathbf{R}f](t, \theta)$ with convolving kernel $\nu(t, \theta)$ may be written as the 2-D convolution of $f(x)$ with the back-projection of $\nu(t, \theta)$.

Denoting the 2-D inverse Fourier transform as $F_2^{-1}\{\cdot\}$, (A.3) may be written as

$$\begin{aligned}\xi(d, R, \lambda) &= d^2 \left[F_2^{-1} \left\{ F_p^2(\rho, \psi) \frac{1}{|\rho|} \right\} \right] (\mathbf{x})|_{\mathbf{x}=\mathbf{0}} = d^2 \int_0^\pi \int_{-\infty}^\infty F_p^2(\rho, \psi) d\rho d\psi \\ &= d^2 R^4 \int_0^\pi \int_{-\infty}^\infty S_p^2(R\rho h(\lambda, \psi)) d\rho d\psi.\end{aligned}\quad (\text{A.5})$$

The last line follows because $f(\mathbf{x})$ is the result of applying the scaling and stretching transformations in (8)–(10) to the circular object $s(\mathbf{x})$, and from Table 2 and $h(\lambda, \psi)$ defined in (13),

$$F_p(\rho, \psi) = R^2 S_p(R\rho h(\lambda, \psi)). \quad (\text{A.6})$$

Note that from (A.5) the Radon space energy ξ_s of the reference object $s_p(\rho)$ is

$$\xi_s = \xi(1, 1, 1) = \int_0^\pi \int_{-\infty}^\infty S_p^2(\rho) d\rho d\psi = \pi \int_{-\infty}^\infty S_p^2(\rho) d\rho. \quad (\text{A.7})$$

Now by a change of variable, (A.5) may be written as

$$\xi(d, R, \lambda) = d^2 R^3 \int_0^\pi \{h(\lambda, \psi)\}^{-1} d\psi \int_{-\infty}^\infty S_p^2(\rho) d\rho = d^2 R^3 q(\lambda) \xi_s, \quad (\text{A.8})$$

where $q(\lambda)$ is defined in (12).

Appendix B. Geometry parameter ambiguity function

To simplify the notation, let the subscripts a and m correspond to the actual object (characterized by R_a, λ_a, ϕ_a) and modeled object (characterized by R, λ, ϕ), respectively. The ambiguity function in (16) may then be expressed as

$$a(R, \lambda, \phi; R_a, \lambda_a, \phi_a) = \frac{2d^2}{N_o} \int_0^\pi \int_{-\infty}^\infty g_a(t, \theta) g_m(t, \theta) dt d\theta - \frac{d^2}{N_o} \int_0^\pi \int_{-\infty}^\infty g_m^2(t, \theta) dt d\theta. \quad (\text{B.1})$$

The first term may be interpreted as a convolution back-projection operation (equation (5)) evaluated at the origin, and the second term may be rewritten using (11),

$$\begin{aligned}a(R, \lambda, \phi; R_a, \lambda_a, \phi_a) &= \frac{2d^2}{N_o} \mathbf{B}[g_a * g_m](\mathbf{x})|_{\mathbf{x}=\mathbf{0}} - \frac{d^2}{N_o} R^3 q(\lambda) \xi_s \\ &= \frac{2d^2}{N_o} \mathbf{B}[\mathbf{R}f_a * \mathbf{R}f_m](\mathbf{x})|_{\mathbf{x}=\mathbf{0}} - \frac{\xi_a}{N_o} \left[\frac{q(\lambda)}{q(\lambda_a)} \left(\frac{R}{R_a} \right)^3 \right],\end{aligned}\quad (\text{B.2})$$

where \mathbf{R} and \mathbf{B} denote the Radon transformation and back-projection operators in (1) and (5), $*$ denotes 1-D convolution with respect to the t variable, and the actual object energy ξ_a is given in (18). Using the equality in (A.4), denoting the 2-D inverse Fourier transform by $F_2^{-1}\{\cdot\}$, and letting $F_a(\rho, \psi)$ and $F_m(\rho, \psi)$

denote the 2-D Fourier transform of the actual and modeled objects in polar coordinates,

$$\begin{aligned}
a(R, \lambda, \phi; R_a, \lambda_a, \phi_a) &= \frac{2d^2}{N_o} \left[f_a ** f_m ** \frac{1}{|r|} \right] (\mathbf{x})|_{\mathbf{x}=\mathbf{0}} - \frac{\xi_a}{N_o} \left[\frac{q(\lambda)}{q(\lambda_a)} \left(\frac{R}{R_a} \right)^3 \right] \\
&= \frac{2d^2}{N_o} \left[F_2^{-1} \left\{ F_a(\rho, \psi) F_m(\rho, \psi) \frac{1}{|\rho|} \right\} \right] (\mathbf{x})|_{\mathbf{x}=\mathbf{0}} - \frac{\xi_a}{N_o} \left[\frac{q(\lambda)}{q(\lambda_a)} \left(\frac{R}{R_a} \right)^3 \right] \\
&= \frac{2d^2}{N_o} \int_0^\pi \int_{-\infty}^\infty F_a(\rho, \psi) F_m(\rho, \psi) d\rho d\psi - \frac{\xi_a}{N_o} \left[\frac{q(\lambda)}{q(\lambda_a)} \left(\frac{R}{R_a} \right)^3 \right]. \tag{B.3}
\end{aligned}$$

The actual and modeled objects are obtained from the circular object $s(\mathbf{x})$ (or $s_p(r)$ in polar coordinates) with 2-D Fourier transform $S(\omega)$ (or $S_p(\rho)$ in polar coordinates) by application of the coordinate transformations in (8)–(10). Using the Fourier transform relationships in Table 2,

$$\begin{aligned}
a(R, \lambda, \phi; R_a, \lambda_a, \phi_a) &= \frac{2d^2}{N_o} \int_0^\pi \int_{-\infty}^\infty R_a^2 S_p(\rho R_a h(\lambda_a, \psi + \phi_a)) R^2 S_p(\rho R h(\lambda, \psi + \phi)) d\rho d\psi \\
&\quad - \frac{\xi_a}{N_o} \left[\frac{q(\lambda)}{q(\lambda_a)} \left(\frac{R}{R_a} \right)^3 \right] \\
&= \frac{\xi_a}{N_o} \left[\frac{2}{q(\lambda_a) \xi_s} \left(\frac{R}{R_a} \right)^2 \int_0^\pi \int_{-\infty}^\infty S_p(\rho h(\lambda_a, \psi)) S_p\left(\frac{\rho R}{R_a} h(\lambda, \psi + \phi - \phi_a)\right) d\rho d\psi \right. \\
&\quad \left. - \frac{\xi_a}{N_o} \left[\frac{q(\lambda)}{q(\lambda_a)} \left(\frac{R}{R_a} \right)^3 \right] \right], \tag{B.4}
\end{aligned}$$

where the last line follows by a change of variable.

Appendix C. Size estimate Cramer–Rao bound

Consider an arbitrary (not necessarily Gaussian) circular object $s_p(r)$ with Hankel transform $S_p(\rho)$. The size estimation ambiguity function is the special case of (17)–(19) where $\lambda = \lambda_a = 1$ and $\Delta\phi = 0$. It may be expressed as

$$a(R, R_a) = \frac{2\xi_a}{\xi_s N_o} \left(\frac{R}{R_a} \right)^2 \int_0^{2\pi} \int_0^\infty S_p(\rho) S_p\left(\frac{\rho R}{R_a}\right) d\rho d\psi - \frac{\xi_a}{N_o} \left(\frac{R}{R_a} \right)^3. \tag{C.1}$$

Let the first two partial derivatives of $S_p(\rho)$ with respect to ρ be denoted by $S'_p(\rho)$ and $S''_p(\rho)$. The second partial derivative of $a(R, R_a)$ in (C.1) is given by

$$\begin{aligned}
\frac{\partial^2 a(R, R_a)}{\partial R^2} &= \frac{\xi_a}{N_o} \left[\frac{4\pi}{\xi_s} \left(\frac{R}{R_a} \right)^2 \int_0^\infty \left(\frac{\rho}{R_a} \right)^2 S_p(\rho) S''_p\left(\frac{\rho R}{R_a}\right) d\rho \right. \\
&\quad + \frac{16\pi R}{\xi_s R_a^2} \int_0^\infty \left(\frac{\rho}{R_a} \right) S_p(\rho) S'_p\left(\frac{\rho R}{R_a}\right) d\rho \\
&\quad \left. + \frac{8\pi}{\xi_s R_a^2} \int_0^\infty S_p(\rho) S_p\left(\frac{\rho R}{R_a}\right) d\rho - \frac{6R}{R_a^3} \right]. \tag{C.2}
\end{aligned}$$

The CRLB on the size estimate error variance may then be written in terms of the size log likelihood function as

$$\sigma_R^2 \geq \left[-E \left\{ \frac{\partial^2 L(R)}{\partial R^2} \right\} \right]^{-1} = - \left[\left\{ \frac{\partial^2 a(R, R_a)}{\partial R^2} \right\}_{R=R_a} \right]^{-1} = \frac{N_o}{2d^2 R_a (3\xi_s - \zeta)}, \quad (C.3)$$

where the expected value of $L(R)$ has been replaced by $a(R, R_a)|_{(R=R_a)}$ which follows from (15) and (16), and where

$$\zeta \doteq 2\pi \int_0^\infty S_p(\rho) [2S_p(\rho) + 4\rho S_p'(\rho) + \rho^2 S_p''(\rho)] d\rho. \quad (C.4)$$

For the special case of the Gaussian object in (20), ζ in (C.4) equals $(\pi/2)^{2.5}$, $\xi_s = \xi_g$ in (22) and the CRLB becomes

$$\sigma_R^2 \geq \left(\frac{2}{\pi} \right)^{2.5} \left[\frac{N_o}{22d^2 R_a} \right] \quad (C.5)$$

or after normalizing,

$$\left(\frac{\sigma_R}{R_a} \right)^2 \geq \frac{2}{11} \frac{N_o}{\xi_a}, \quad (C.6)$$

where $\xi_a = d^2 R_a^3 \xi_g$ is the actual object Radon transform energy in (18).

References

- [1] R. Bracewell, *The Fourier Transform and its Applications*, McGraw-Hill, New York, 1965.
- [2] D.B. Cooper, H. Elliott, F. Cohen, L. Reiss and P. Symosek, "Stochastic boundary estimation and object recognition", *Comput. Graphics Image Process.*, Vol. 12, 1980, pp. 326-356.
- [3] B. Cornuelle, "Acoustic Tomography", *IEEE Trans. Geosci. Remote Sensing*, Vol. GE-20, July 1982, pp. 326-332.
- [4] W.D. Daily, Guest Editor, "Special Section on Geotomography", *Proc. IEEE*, Vol. 74, February 1986, pp. 328-360.
- [5] M.E. Davison and F.A. Grunbaum, "Tomographic reconstruction with arbitrary directions", *Commun. Pure Appl. Math.*, Vol. 34, 1981, pp. 77-120.
- [6] R. Guzzardi, G. Licitra and M.R. Voegelin, "Recent developments in Compton tomographic imaging of the lung and possible application to object recognition", *IEEE Trans. Nucl. Sci.*, Vol. NS-34, June 1987, pp. 667-671.
- [7] G.T. Herman, Guest Editor, "Special Issue on Computerized Tomography", *Proc. IEEE*, Vol. 71, March 1983, pp. 291-431.
- [8] D.G. Luenberger, *Introduction to Linear and Nonlinear Programming*, Addison-Wesley, Reading, MA, 1973.
- [9] R.J. Lytle and M.R. Portnoff, "Detecting high-contrast seismic anomalies using cross-borehole probing", *IEEE Trans. Geosci. Remote Sensing*, Vol. GE-22, March 1984, pp. 93-98.
- [10] R.L. Parker, "Understanding inverse theory", *Ann. Rev. Earth Planet. Sci.*, Vol. 5, 1977, pp. 35-64.
- [11] D. Rossi, "Reconstruction from projections based on detection and estimation of objects", Ph.D. Dissertation, Department of Electrical Engineering and Computer Science, M.I.T., Cambridge, MA, August 1982.
- [12] D. Rossi and A. Willsky, "Reconstruction from projections based on detection and estimation of objects", *IEEE Trans. Acoust., Speech Signal Process.*, Vol. ASSP-32, August 1984, pp. 886-906.
- [13] S.W. Rowland, "Computer implementation of image reconstruction formulas", in: G.T. Herman, ed., *Image Reconstruction from Projections—Implementation and Applications*, (Topics in Applied Physics, Vol. 32), Springer-Verlag, New York, 1979.
- [14] L.A. Santalo, "Integral geometry and geometric probability," in: G. Rota, ed., *Encyclopedia of Mathematics and its Applications*, Addison-Wesley, Reading, MA, 1976.
- [15] D.L. Snyder, "Utilizing side information in emission tomography", *IEEE Trans. Nucl. Sci.*, Vol. NS-31, Feb. 1984, pp. 533-537.
- [16] D.M. Spielman, "Detection and estimation of objects from noisy projection measurements", Report No. LIDS-TH-1323, Laboratory for Information and Decision Systems, M.I.T., Cambridge, MA, August 1983.
- [17] T. Tomitani, "An edge detection algorithm for attenuation correction emission CT", *IEEE Trans. Nucl. Sci.*, Vol. NS-34, February 1987, pp. 309-312.
- [18] H. Van Trees, *Detection, Estimation, and Modulation Theory, Part I*, Wiley, New York, 1968.